# Proximity-induced caspase-9 activation on a DNA origami-based synthetic apoptosome

*Citation for published version (APA):*
Rosier, B., Markvoort, A. J., Gumi Audenis, B., Roodhuizen, J., den Hamer, A., Brunsveld, L., & de Greef, T. F. A. (2020). Proximity-induced caspase-9 activation on a DNA origami-based synthetic apoptosome. *Nature Catalysis*, *3*(3), 295-306. https://doi.org/10.1038/s41929-019-0403-7

*Document license:*
TAVERNE

*DOI:*
10.1038/s41929-019-0403-7

*Document status and date:*
Published: 01/03/2020

*Document Version:*
Publisher’s PDF, also known as Version of Record (includes final page, issue and volume numbers)

***Please check the document version of this publication:***

• A submitted manuscript is the version of the article upon submission and before peer-review. There can be important differences between the submitted version and the official published version of record. People interested in the research are advised to contact the author for the final version of the publication, or visit the DOI to the publisher's website.
• The final author version and the galley proof are versions of the publication after peer review.
• The final published version features the final layout of the paper including the volume, issue and page numbers.

Link to publication

*General rights*
Copyright and moral rights for the publications made accessible in the public portal are retained by the authors and/or other copyright owners and it is a condition of accessing publications that users recognise and abide by the legal requirements associated with these rights.

- Users may download and print one copy of any publication from the public portal for the purpose of private study or research.
- You may not further distribute the material or use it for any profit-making activity or commercial gain
- You may freely distribute the URL identifying the publication in the public portal.

If the publication is distributed under the terms of Article 25fa of the Dutch Copyright Act, indicated by the “Taverne” license above, please follow below link for the End User Agreement:

www.tue.nl/taverne

*Take down policy*
If you believe that this document breaches copyright please contact us at:

openaccess@tue.nl

providing details and we will investigate your claim.

Download date: 04. Oct. 2023

nature catalysis

ARTICLES
https://doi.org/10.1038/s41929-019-0403-7

# Proximity-induced caspase-9 activation on a DNA origami-based synthetic apoptosome

Bas J. H. M. Rosier[1,2], Albert J. Markvoort[2,3], Berta Gumí Audenis[2,4], Job A. L. Roodhuizen[2,3], Anniek den Hamer[1,2], Luc Brunsveld[1,2]* and Tom F. A. de Greef[1,2,3,5]*

**Living cells regulate key cellular processes by spatial organization of catalytically active proteins in higher-order signalling complexes. These act as organizing centres to facilitate proximity-induced activation and inhibition of multiple intrinsically weakly associating signalling components, which makes elucidation of the underlying protein–protein interactions challenging. Here we show that DNA origami nanostructures provide a programmable molecular platform for the systematic analysis of signalling proteins by engineering a synthetic DNA origami-based version of the apoptosome, a multiprotein complex that regulates apoptosis by colocalizing multiple caspase-9 monomers. Tethering of both wild-type and inactive caspase-9 variants to a DNA origami platform demonstrates that enzymatic activity is induced by proximity-driven dimerization with half-of-sites reactivity and, furthermore, reveals a multivalent activity enhancement in oligomers of three and four enzymes. Our results offer fundamental insights in caspase-9 activity regulation and demonstrate that DNA origami-based protein assembly platforms have the potential to inform the function of other multi-enzyme complexes involved in inflammation, innate immunity and cell death.**

Nanoscale organization of interacting proteins is a key regulatory principle in signalling pathways that are involved in all major cell events, including apoptosis, metabolism, inflammation and immunity[1,2]. Inactive enzymes with a low intrinsic affinity that are present at low intracellular concentrations can be physically assembled into well-defined higher-order signalling complexes[3] or open-ended assemblies[4]. Dedicated scaffold proteins serve as supramolecular organizing centres (SMOCs), facilitating protein–protein interactions with precise control over the position and orientation of the individual components (Fig. 1a)[5]. Efforts to address and rewire SMOC-based signalling complexes have provided important structural and functional understanding into the underlying design principles[6–8]. In general, experimental and theoretical work illustrate that colocalization of signalling components promotes proximity-induced enzyme activation through weak non-covalent interactions, thereby overcoming signal thresholds, increasing pathway robustness and shaping response dynamics[9–11].

Bottom-up approaches that employ synthetic platforms enable systematic analysis and full control over the number, position and orientation of interacting components, providing an excellent strategy to further unravel the molecular mechanisms behind spatial organization in signalling pathways[12,13]. The programmability of DNA and its inherent biocompatibility enables rational design of defined synthetic architectures for the construction of protein–DNA hybrid systems[14–17]. DNA origami-based nanostructures in particular are well-suited as synthetic platforms as their unique addressability allows for precise assembly of multiple non-identical proteins with nanometre accuracy[18–20]. The DNA origami technique has found broad applicability as an experimental tool for spatial organization of native multiprotein systems, such as amyloid fibrils[21], membrane fusion proteins[22], nucleosomes[23,24] and intrinsically disordered proteins[25]. Furthermore, these platforms have been used to engineer localized genetic circuits[26], to study confinement-induced enzyme activity[27,28] and to investigate scaffolded metabolic cascades[29–33]. Although these studies have elegantly applied the programmability of DNA nanotechnology to facilitate the organization of, for example, structural protein assemblies and metabolic enzymes with small-molecule substrates, a DNA nanostructure-based platform for directly probing protein–protein interactions between catalytically active intracellular signalling components is currently lacking.

Here we present a DNA-based synthetic SMOC for studying proximity-induced protein–protein interactions that are involved in intracellular signal transduction. We construct DNA origami-based synthetic variants of the apoptosome; that is, a 27-nm-diameter, sevenfold-symmetric multiprotein complex that is involved in the intrinsic apoptotic pathway. In the cell, mitochondrial outer membrane permeabilization and subsequent release of cytochrome *c* induces the assembly of the apoptosome, which recruits the cysteine-dependent aspartic protease, caspase-9, to initiate a cascade of proteolytic activity that eventually leads to programmed cell death[34]. Previous works suggest that the apoptosome recruits up to four caspase-9 monomers through caspase recruitment domains (CARDs), after which dimerization contributes to a dramatic increase in enzyme activity (Fig. 1b)[35–37]. By mimicking the scaffolding function of the apoptosome with a DNA origami platform[18], we can assemble individual caspase-9 monomers with absolute control over their position, using the hybridization of DNA-functionalized enzymes to protrude single-stranded handles on the DNA origami surface (Fig. 1c). Using a bottom-up approach, our in vitro studies reveal that caspase-9 activity is induced by proximity-driven dimerization, driven by an increase in effective concentration as a

---

[1]Laboratory of Chemical Biology, Department of Biomedical Engineering, Eindhoven University of Technology, Eindhoven, the Netherlands. [2]Institute for Complex Molecular Systems, Eindhoven University of Technology, Eindhoven, the Netherlands. [3]Computational Biology Group, Department of Biomedical Engineering, Eindhoven University of Technology, Eindhoven, the Netherlands. [4]Laboratory of Self-Organising Soft Matter and Laboratory of Macromolecular and Organic Chemistry, Department of Chemical Engineering and Chemistry, Eindhoven University of Technology, Eindhoven, the Netherlands. [5]Institute for Molecules and Materials, Radboud University, Nijmegen, the Netherlands. *e-mail: l.brunsveld@tue.nl; t.f.a.d.greef@tue.nl

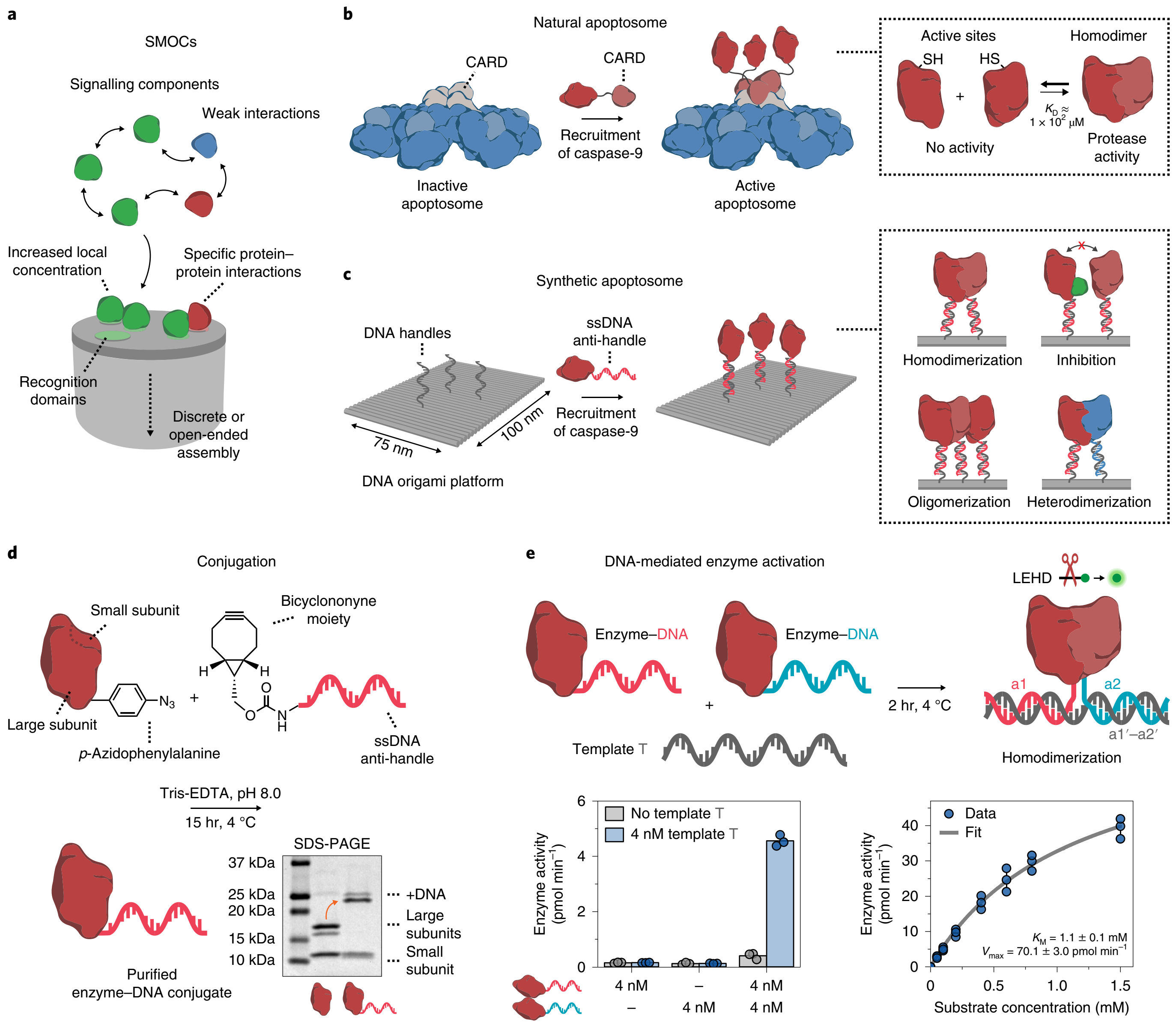

**Fig. 1 | General concept and design elements for the construction of a DNA-based synthetic apoptosome. a**, A schematic concept of SMOCs. **b**, A schematic drawing of the natural apoptosome that functions by assembling inactive caspase-9 monomers through CARDs. The increase in local concentration induces caspase-9 dimerization, leading to proteolytic cleavage of downstream caspases and eventually apoptosis. **c**, A schematic drawing of the DNA origami-based synthetic apoptosome. Single-stranded DNA (ssDNA) handles on the DNA origami surface recruit caspase-9 monomers with full control over the number, position and relative geometry, allowing for the characterization of specific protein–protein interactions such as homodimerization, inhibition, oligomerization and heterodimerization. **d**, A reaction scheme for the conjugation of caspase-9 to an oligonucleotide anti-handle. Caspase-9 was expressed in *Escherichia coli* with unnatural amino acid *p*-azidophenylalanine at the N-terminus and reacted with a BCN-DNA (8 kDa). Purification with affinity chromatography afforded pure enzyme–DNA conjugates, as shown by SDS-PAGE analysis. Mature caspase-9 consists of a non-covalently bound N-terminal large (18.3 and 19.2 kDa) and C-terminal small subunit (12.8 kDa), which are separated during gel analysis (see also Supplementary Fig. 4). The identity of all of the protein fragments was confirmed using mass spectrometry analysis (Supplementary Fig. 2). **e**, Bivalent template T was used to induce dimerization of two identical caspase-9 monomers with different DNA sequences (a1 and a2, indicated by red and blue, respectively). The enzyme activity (left graph) was measured using stoichiometric amounts of all three components and 167 μM of the synthetic caspase substrate LEHD–AFC (Supplementary Fig. 8), whereas enzyme kinetics (right graph) was determined by measuring activity at 4 nM of each enzyme–DNA conjugate and varying concentrations of the substrate (0–1.5 mM). The data was fitted with the standard Michaelis–Menten expression (see Methods). The bars represent the mean enzyme activity. All of the experiments were performed in independent triplicates. $K_M$, Michaelis constant; $V_{max}$, maximum rate.

result of tethering of the components to the platform. We then construct three- and four-enzyme systems to study the effect of higher-order clustering on caspase-9 activity. By combining experimental and theoretical results, we analyse kinetic data considering possible effects such as enzyme incorporation efficiency and statistical factors, and suggest a multivalent catalytic effect leading to enhanced activity in caspase-9 oligomers. Finally, we provide direct evidence that the enzymatic activity of a heterodimer consisting of a wild-type monomer and an active-site mutant, is similar to the activity of the wild-type homodimer, confirming the hypothesis that conformational changes in the active sites of a caspase-9 homodimer proceed via an asymmetric mechanism[38]. Our experimental platform demonstrates that systematic in vitro analysis of native protein–protein interactions using DNA-based synthetic SMOCs can facilitate the discovery of new molecular mechanisms in proximity-driven enzyme regulation.

## Results

**Activity of DNA-functionalized caspase-9.** Enzyme–DNA conjugates were synthesized to construct a DNA origami-based platform that allows for programmable caspase-9 organization[20,39]. Full-length caspase-9 monomers consist of an N-terminal CARD that is connected to the catalytic domain via a long flexible linker (Fig. 1b)[38]. Crystal structures show that on recruitment, CARDs on the apoptosome interact with caspase-9 CARDs to form a well-defined three-dimensional complex, to which multiple caspase-9 catalytic domains are tethered flexibly[36,37]. Replacing the CARD domain of caspase-9 with an oligonucleotide enables incorporation of the catalytic domain onto DNA nanostructures and mimics the recruiting function of the CARD using hybridization to complementary single-stranded handles on the DNA origami surface (Fig. 1b,c). The specific protein–protein interactions involved in caspase-9 activation warrant stoichiometric, site-specific oligonucleotide functionalization without the use of large protein helper domains. We therefore incorporated the non-canonical amino acid *p*-azidophenylalanine at the N-terminus of the catalytic domain of caspase-9 by using amber codon suppression in *Escherichia coli* with an engineered orthogonal aminoacyl tRNA synthetase/tRNA pair from *Methanococcus jannaschii* (see Methods and Supplementary Figs. 1a and 2a)[40]. The small bioorthogonal azide moiety was used for conjugation to a bicyclononyne-functionalized oligonucleotide (BCN–DNA) using strain-promoted azide–alkyne cycloaddition (Fig. 1d)[41–43]. The oligonucleotide consists of a 10-nucleotide (nt) single-stranded linker that separates the enzyme and a 15-nt anti-handle that is used for hybridization to the handles (Supplementary Table 2 and Supplementary Fig. 3). Analysis using sodium dodecyl sulfate–polyacrylamide gel electrophoresis (SDS-PAGE) confirmed successful conjugation of a single oligonucleotide to the N-terminus of caspase-9 and subsequent purification resulted in the complete removal of all of the unreacted protein and excess BCN–DNA (Fig. 1d, Supplementary Figs. 4 and 6).

As conjugation of oligonucleotides to enzymes can considerably influence catalytic behaviour[44,45], we measured the activity of the caspase-9 enzyme–DNA conjugates. We employed a 30-nt single-stranded template, T, to bring two caspase-9 monomers into close proximity through DNA hybridization[46] and followed proteolytic cleavage of synthetic caspase substrate LEHD–AFC (where AFC is 7-amino-4-(trifluoromethyl)coumarin)[47] over time (Fig. 1e and Methods). We observed a sharp increase in activity only when both enzyme–DNA conjugates and the template are present (Fig. 1e, left graph). This suggests that template T functions as a bivalent scaffold inducing dimerization of caspase-9 by increasing the effective concentration, in a similar manner as protein-based dimerizing scaffolds that are reported in the literature[48–50]. We performed a quantitative kinetic analysis and determined the $K_M$ of the ternary complex comprising the caspase-9 conjugates and template T. The value of $1.1 \pm 0.1$ mM is in the same range as found for caspase-9 activation by the native apoptosome and by other synthetic scaffold platforms (Fig. 1e, right graph)[47]. These results collectively confirm the successful synthesis of functionally active caspase-9 enzyme–DNA conjugates and demonstrate that DNA can be used to facilitate proximity-induced activation.

**DNA origami-mediated caspase-9 enzyme activity.** The native apoptosome is an organizing platform that induces the colocalization of caspase-9 enzymes through seven CARDs. Flexible tethering of caspase-9 through CARD–CARD interactions results in dimerization of the catalytic domains and a subsequent 100–1,000-fold increase in enzyme activity[51,52]. Although crystal structures indicate that up to four caspase-9 monomers bind to the apoptosome simultaneously[36,37], in vitro investigations have so far focused solely on dimerization by employing protein-based bivalent scaffolds or engineering chimeric proteins[48–50]. To assess the effects of multivalent enzyme clustering, we constructed a synthetic DNA-based version of the apoptosome using a twist-corrected rectangular DNA origami nanostructure[18], on which the location of an arbitrary number of caspase-9 monomers can be tightly controlled (see Methods and the 'self-assembly of DNA origami nanostructures' section in the Supplementary Methods). In our design, we substitute the structural proteins of the apoptosome with a DNA nanostructure and replace the recruiting function of the CARDs by DNA–DNA hybridization. As such, several features of the native system that could modulate caspase-9 activation and regulation are not taken into account; for example, recent work has indicated that allosteric interactions of the catalytic domain of caspase-9 with its CARD, the flexible linkers and the apoptosome itself can affect enzyme activity[36,53,54]. However, we argue that a modular DNA-based model system composed of a controlled number of catalytic domains with well-defined interactions can help isolate the key molecular determinants of caspase-9 regulation.

The unique addressability of DNA origami allows for programmable positioning of the handles with ~6 nm resolution across the entire platform (Fig. 2a). Atomic force microscopy (AFM) confirmed the self-assembly of $75 \times 100$ nm$^2$ DNA origami nanostructures and revealed that individual 4.5-nm diameter, 32-kDa caspase-9 monomers can be observed on the DNA origami surface (Fig. 2b and Supplementary Fig. 13). Analysis of 260 well-formed one-enzyme DNA nanostructures revealed an average enzyme incorporation efficiency of 76% (Supplementary Fig. 16c), which is similar to values reported in the literature[55,56]. Next we designed two-enzyme DNA nanostructures with varying distances between two caspase-9 monomers that are arranged either parallel (Fig. 2c, top row) or perpendicular (bottom row) to the DNA helical axis, and used agarose gel electrophoresis (Supplementary Fig. 12) and AFM imaging (Fig. 2c, Supplementary Figs. 14 and 15) to analyse the integrity of the structures. When monomer separation is large (that is, >20 nm), two individual spots can be distinguished in the AFM images, indicating faithful incorporation of caspase-9 at the pre-programmed positions, as well as physical separation of the monomers by the DNA nanostructure. By contrast, only a single spot is discerned at smaller separation distances (<20 nm), with the shape and intensity of these features suggesting the presence of two adjacent caspase-9 monomers (Supplementary Fig. 16a,b). We attribute this observation to a combination of the limited resolution of the imaging technique and intermolecular interactions (both specific and non-specific, see below) between the enzymes. Visual inspection of the AFM images allows straightforwards identification of DNA nanostructures with either one or two enzymes (Fig. 2c, compare, for example, 12 and 24 nm on the bottom row). The enzyme incorporation efficiency per handle was found to be approximately 75% per handle for all of the samples, irrespective of monomer separation (Fig. 2c, Supplementary Fig. 16c). Although this contrasts with previous work that reported a diminished incorporation when two enzymes were brought into close proximity on a similar DNA origami scaffold[30], we hypothesize that the attractive interaction between two caspase-9 monomers balances possible steric effects at small separation distances, leading to an overall constant incorporation efficiency. Taken together, the results of the AFM analysis confirm that DNA nanostructures that contain two caspase-9 monomers can be constructed with tight control over the position of—and distance between—tethered monomers.

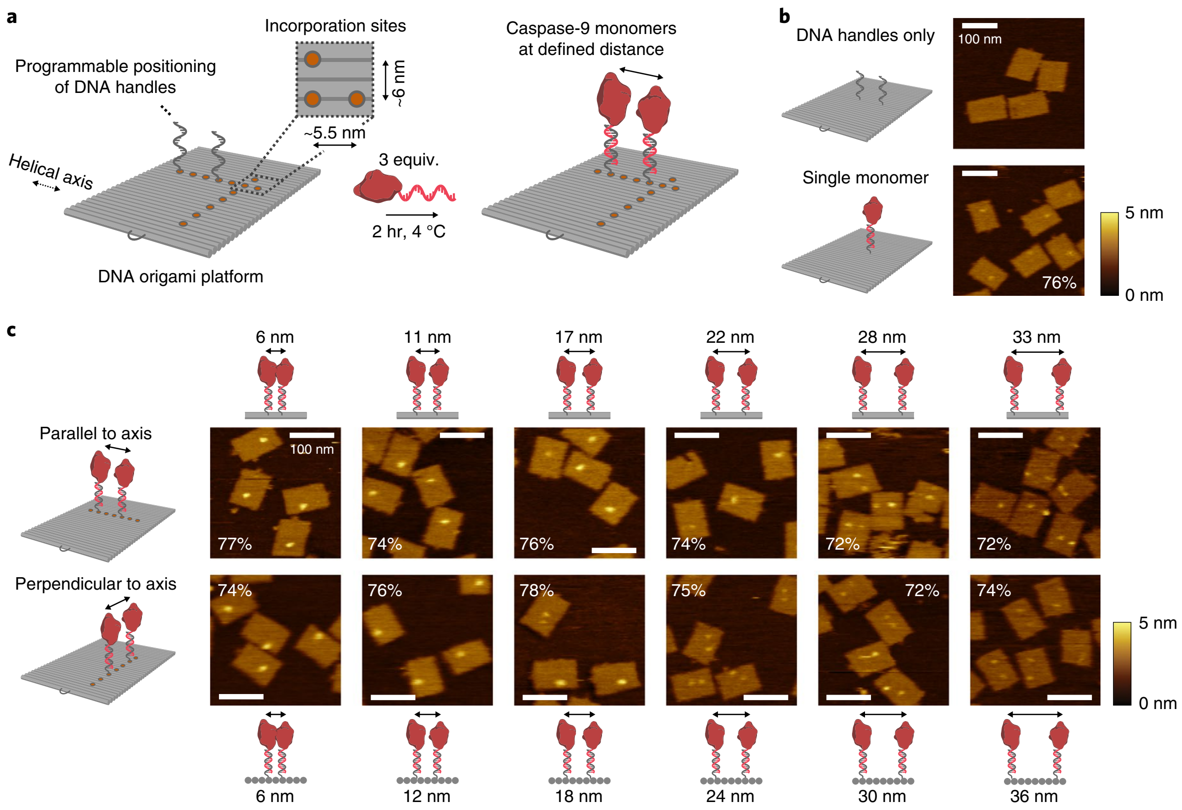

**Fig. 2 | Characterization of caspase-9 assembly onto DNA origami nanostructures.** **a**, A schematic of the general strategy for caspase-9 incorporation on DNA origami platforms. By including appropriate handle-extended staple strands during the self-assembly process, the position of—and distance between—two ssDNA handles can be controlled. Specifically, the DNA origami technique enables a minimal distance between incorporation sites (orange circles) of 5.5 nm parallel and 6 nm perpendicular to the DNA helical axis (see the 'self-assembly of DNA origami nanostructures' section in the Supplementary Methods). Incubation of complementary enzyme–DNA conjugates leads to hybridization and incorporation of two caspase-9 monomers at defined distances. Typically, 4 nM DNA origami was incubated with 3 equiv. of enzyme–DNA conjugate per handle for 2 hr at 4 °C. For AFM imaging, functionalized nanostructures were purified using 1.5% agarose gel extraction. **b**,**c**, Topographic AFM (tapping mode in solution) images of control samples (**b**) and DNA origami nanostructures functionalized with two 32-kDa caspase-9 monomers (**c**) at various distances that are parallel (top row) and perpendicular (bottom row) to the helical axis. The caspase-9 incorporation efficiency per handle is indicated as a percentage, and was calculated based on at least 250 well-formed nanostructures using four different images per sample. Colour bars indicate the height scale in AFM images. Scale bars, 100 nm.

We then assessed if caspase-9 displays functional enzymatic activity when assembled on DNA origami nanostructures. As proximity-induced activation of caspase-9 involves dimerization, we envisioned that the activity can be tuned by varying the distance between the monomers. To this end we assembled two-enzyme DNA nanostructures with monomer separations that vary between 6 and 36 nm, and followed proteolytic activity over time (see Fig. 3a,b and Methods). The highest enzyme activity was observed when the monomers were in closest proximity, after which the activity dropped sharply and approached background activity levels for separations >20 nm (Fig. 3b). Although we use a twist-corrected version of the DNA origami rectangle[18] that adopts the designed shape when deposited on a surface for AFM imaging (Fig. 2), theoretical and experimental studies have determined that the single-layer DNA nanostructure can still exhibit moderate flexibility in solution (Supplementary Fig. 9)[57,58]. To exclude that this structural flexibility has an effect on the distance-dependent performance of our system, we compared enzyme activity in two different arrangements of the caspase-9 monomers (Fig. 3b). Enzyme monomers arranged either parallel to the rigid DNA helical axis (with an expected persistence length >40 nm, ref. [59]) or perpendicular to the axis displayed similar distance-dependent behaviour (Fig. 3b, compare the top and bottom graphs), indicating that local fluctuations in protein positions do not have an influence on enzymatic activity. Increasing the single-stranded DNA linker between the enzyme and handle from 10 to 15 nt slightly decreased the maximum activity while retaining distance-dependent behaviour, illustrating that enzyme activation requires tight colocalization of the monomers and that the DNA-based assembly method does not introduce adverse steric effects (Supplementary Fig. 18).

After correcting for background activity and incorporation efficiency as determined by AFM, DNA origami-mediated caspase-9 activation at 6-nm monomer separation resulted in a 23-fold increase in enzyme activation, equivalent to dimerization enforced by the bivalent template T (Fig. 3c; see Methods for data correction). This activity increase is in the same range as reported in literature for other engineered systems for caspase-9 activation, which obtained fold change values in the range of 3–90 (refs. [36,47,49,50]), indicating that DNA-based induction of caspase-9 activity represents a viable strategy for investigating its catalytic function. Although native apoptosome-mediated activation of caspase-9 results in a two-to-three-orders-of-magnitude upregulation of activity[51], our results are comparable with reported activity profiles of in vitro reconstituted native apoptosomes when using the same synthetic substrate[47]. Taken together, even though the synthetic DNA-based design does not capture all molecular determinants that contribute to caspase-9 activation by the apoptosome, our results demonstrate that proximity-induced dimer formation

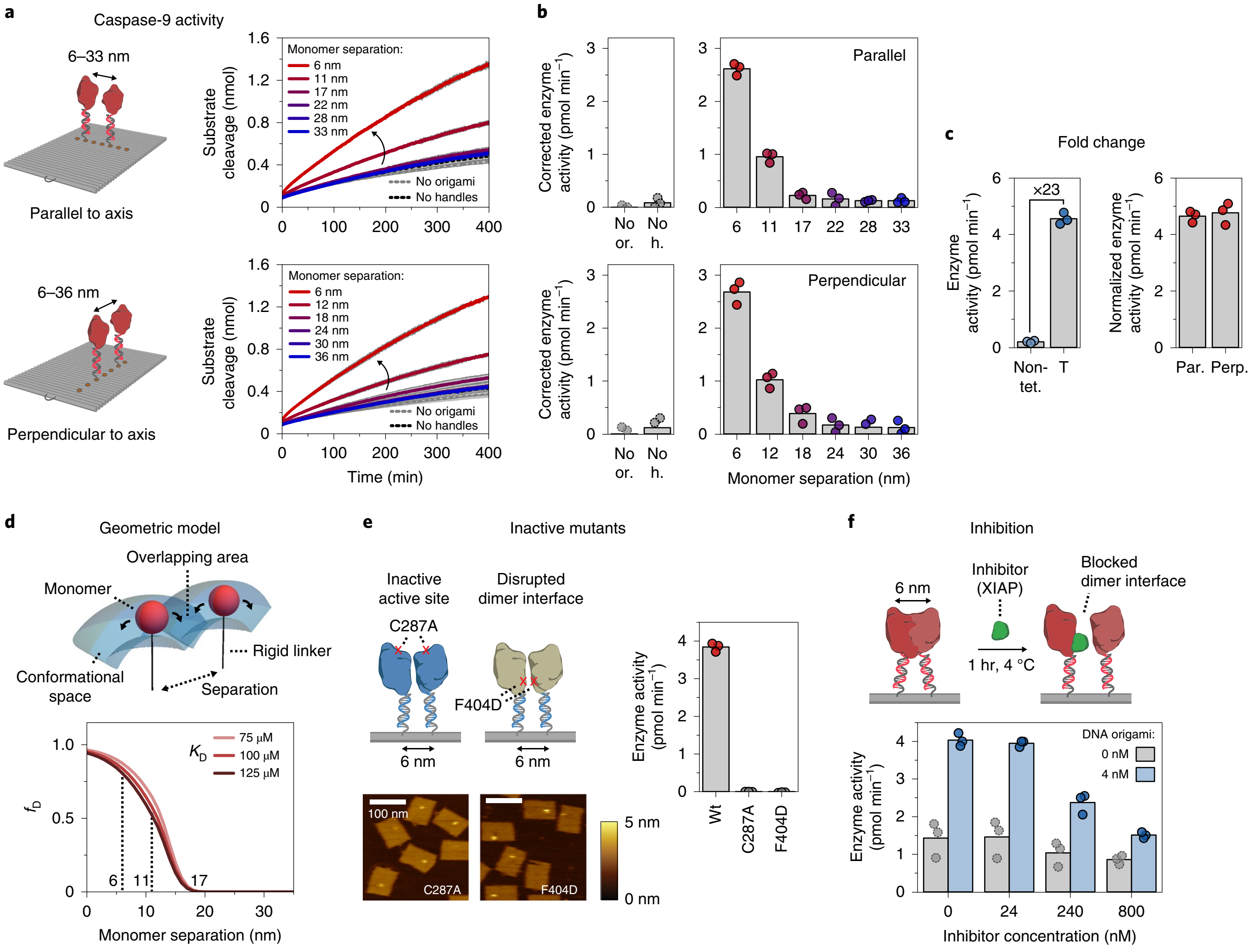

**Fig. 3 | Activation of caspase-9 occurs by distance-dependent dimerization of tethered monomers. a**,**b**, Distance-dependent enzyme activity of two caspase-9 monomers on DNA origami nanostructures parallel (top) and perpendicular (bottom) to the DNA helical axis. Data in **a** are represented as mean ± s.d. of three independent experiments. The enzyme activity (**b**) was calculated from the initial slope of the time traces in **a** and corrected by subtracting the mean background activity (no or.). No or., no DNA origami present; no h., DNA origami without handles. **c**, The fold change in enzyme activity for T, and 6-nm samples parallel (par.) and perpendicular (perp.) to DNA origami helical axis was calculated by comparison with 4 nM non-tethered (non-tet.) caspase-9 in buffer. The activity of DNA origami samples was normalized based on an incorporation efficiency per handle of 75%. **d**, A three-dimensional geometric model that assumes free movement for each tethered monomer in the conformational space is shown, as determined by molecular dynamics simulations. The tethered $f_D$ was plotted as a function of the dissociation constant of caspase-9 dimerization in solution ($K_D$) and the separation between the tethered monomers. **e**, AFM images show correct incorporation of caspase-9 point mutants C287A and F404D on DNA origami nanostructures at 6 nm monomer separation, but both mutants exhibit no enzymatic activity. Colour bars indicate the height scale in AFM images. Scale bars, 100 nm. Wt. wildtype. **f**, The inhibition of caspase-9 by various concentrations of XIAP in the absence (grey) or presence (blue) of 4 nM 6-nm two-enzyme DNA nanostructures. Reactions were carried out with 4 nM DNA origami (unless indicated otherwise) and 3 equiv. of enzyme–DNA conjugate per handle, and incubated for 2 h at 4 °C. The activity was determined by monitoring cleavage of 167 µM LEHD–AFC at 18 °C. All experiments were performed in independent triplicates. Individual data points are represented as circles, whereas bars represent mean activity.

and subsequent induction of catalytic activity plays a major role in the native system.

We performed several essential control experiments to validate DNA origami nanostructures as inert assembly platforms. First, a control in which DNA origami without handles was used exhibited only background activity, confirming that the DNA nanostructures do not influence caspase-9 function (Fig. 3b, compare the dotted grey and black circles). Next we assessed the influence of altered pH near the surface of the negatively charged DNA origami structure[60] by measuring enzyme activity both in solution and mediated by the 6-nm two-enzyme DNA nanostructure at varying pH levels. Both experiments revealed a bell-shaped pH dependence with an optimum at pH 7.0 (ref. [61]), suggesting that the behaviour of tethered caspase-9 near the surface of the DNA origami platform is not affected by local changes in pH (Supplementary Fig. 19). Finally, we determined the kinetic parameters of the 6-nm two-enzyme DNA nanostructure and found a $K_M$ of 1.8 ± 0.1 mM and a $V_{max}$ of 51.5 ± 2.1 pmol min$^{-1}$ (Supplementary Fig. 20). Although $K_M$ is slightly higher and $V_{max}$ slightly lower than the values reported previously for the bivalent template T (Fig. 1e), it is known that immobilization of enzymes on a surface can affect the kinetic parameters, which can be attributed to a lower affinity of the substrate for the enzyme due to diffusional limitations or conformational changes of the enzyme near the surface[62]. These results collectively establish DNA origami nanostructures as a platform for the assembly of physically interacting enzymes such as caspase-9 and the systematic analysis of the effects of relative geometry on enzyme activity.

To further rationalize the experimental results, we constructed a geometric model for two tethered interacting enzymes based on the concept of effective concentration[63] and calculated the fraction of tethered dimer as a function of the distance between the anchor points (Fig. 3d and Methods). Coarse-grained molecular dynamics simulations were employed to define a conformational volume in which the tethered enzymes can move freely (see Supplementary Fig. 21 and the 'molecular dynamics simulations' section in the Supplementary Methods). The model allowed us to calculate the dimerization probability ($f_D$) as a function of monomer separation and the $K_D$ of non-tethered caspase-9 (see Methods)[64]. The results show that at monomer separations greater than 20 nm, the calculated fraction of the dimer approaches zero as the tethered monomers cannot physically interact (Fig. 3d). In accordance with the experimental data, a sharp drop in $f_D$ is observed in the regime between 5 and 15 nm, decreasing from 90% at 5 nm to less than 10% at 15 nm. Although the model does not consider steric effects or the specific mutual orientation of the monomers, it describes the experimental data well, suggesting that caspase-9 dimerization on the DNA origami platform originates from an increase in effective concentration. Taken together, these results confirm that DNA origami-mediated activation of caspase-9 is consistent with proximity-induced homodimerization, and that the extent of activity can be tuned by varying the separation between interacting monomers.

To illustrate the functionality of the DNA origami platforms for studying protein–protein interactions, we investigated the behaviour of caspase-9 mutants and the effect of inhibition on enzyme activity using a biologically relevant inhibitor. First, we expressed and conjugated two caspase-9 point mutants to DNA (Supplementary Figs. 1b,c, 2b,c and 5), resulting in enzyme–DNA conjugates with either a disabled active site (C287A mutant) or a disrupted dimer interface (F404D mutant). Although AFM imaging revealed correct assembly of 6-nm-spaced two-enzyme DNA nanostructures, both mutants did not exhibit enzymatic activity, reaffirming that DNA origami-mediated caspase-9 activation proceeds via a homodimerization mechanism (Fig. 3e and Supplementary Fig. 17). Second, we investigated the response of DNA origami-mediated caspase-9 activity to the BIR3 domain of X-linked inhibitor of apoptosis protein (XIAP), an important human regulatory protein that strongly binds to the C-terminal small subunit of caspase-9 ($K_i < 20$ nM), forming a heterodimeric complex that prevents caspase-9 dimerization[65,66]. After assembly of 6-nm two-enzyme wild-type caspase-9 DNA nanostructures, increasing concentrations of inhibitor were added and protease activity was measured (Fig. 3f). Although the binding affinity of the inhibitor to caspase-9 is in the low nanomolar range, the experiments reveal that very high concentrations (60 equivalents and higher) are needed to effectively inhibit enzyme activity, illustrating the increased effective concentration of caspase-9 on the DNA origami platform. These results together demonstrate that our DNA origami platform can serve as a versatile tool for biochemical analysis of intracellular signalling components and their regulation by other protein, such as inhibitors.

**Clustering of multiple caspase-9 enhances enzymatic activity.** We have demonstrated that caspase-9 dimerization is sufficient to induce activity; however, the apoptosome is hypothesized to bind up to four enzymes simultaneously[35,37,53]. We therefore wondered how clustering of enzymes influences their catalytic activity. Although multivalent effects on enzyme catalysis have not been described in the biochemical literature, previous work by Prins et al. on zinc-based catalysts has revealed that clustering of dimerizing subunits can lead to activity enhancement[67]. The authors developed a theoretical model to show that the activity increase is correlated with a statistical increase in the number of active catalytic units following clustering of subunits in a multivalent system. We constructed several multivalent caspase-9 DNA nanostructures to investigate the effect of oligomerization—including linear ([125]) and triangular ([123]) three-enzyme configurations and a four-enzyme variant ([1234])—and confirmed successful assembly using agarose gel electrophoresis (Supplementary Fig. 22) and AFM imaging (Fig. 4a and Supplementary Fig. 23). For both three-enzyme systems, enzymatic activity increased 96% compared with reference configurations [126] and [256], in which one monomer is positioned such that it cannot interact with the other two monomers (Fig. 4b, top). As expected, the enzyme activity of these reference 2 + 1 configurations was similar to the 6-nm two-enzyme controls. The activity of the four-enzyme [1234] proximal configuration increased by 59% compared with the [1278] distal reference (Fig. 4b, bottom). As the latter can be viewed as a non-interacting pair of two-enzyme systems on the same DNA origami, it exhibited similar activity compared with the two-enzyme controls, as expected (Fig. 4b, bottom). These experimental results collectively demonstrate an increase in proteolytic activity when more than two caspase-9 monomers are brought into close proximity.

We developed a thermodynamic model that describes dimerization of tethered enzymes in two-, three- and four-enzyme configurations to dissect the potential factors that contribute to the observed activity increase. The underlying principle of the model is that two tethered enzymes exist in an equilibrium between two concentration-independent states, either as inactive monomers or as an active dimer, whereas higher-order interactions are not possible (see Fig. 4c and Supplementary Note 1). This allows us to calculate the average number of dimers per DNA origami for each enzyme configuration, which we assume is proportional to the experimentally measured caspase-9 activity. The average number of dimers for the 6-nm two-enzyme DNA nanostructure is simply given by $f_D$ (with a value of approximately 0.9 at 6 nm monomer separation, see Fig. 3c,d), allowing us to express the number of dimers in the other enzyme configurations as a function of system parameter $f_D$. Applying this approach to, for example, the triangular three-enzyme system (which reflects the experimental [123] configuration) we can define four distinct states (one fully monomeric and three symmetric dimeric states) for each of which we derive an expression for the dimer fraction as a function of $f_D$ (Fig. 4d). However, enzyme incorporation onto DNA nanostructures is not 100% in practice, which results in a distribution of species with varying enzyme occupancy; that is, eight different species with 0, 1, 2 or 3 enzymes (Fig. 4e). We systematically derived expressions for the contribution of each species as a function of $f_D$ and incorporation efficiency $p$ (as determined in Fig. 2), with the sum of all contributions representing the average number of dimers per DNA nanostructure (see Supplementary Note 1 for the derivation of all models). Although the model only considers dimerization and does not include any higher-order allosteric effects, the three- and four-enzyme configurations exhibit a moderate increase in the average number of dimers per DNA origami (Fig. 4f; compare the green bars to the red control bars). This effect has a statistical origin and is correlated to an increase in the number of dimerization possibilities compared with a two-enzyme situation. Interestingly, the models predict that the number of dimers in the [123] three-enzyme system is only 55% higher compared with the two-enzyme system, whereas experimentally an approximately twofold increase in activity was observed (Fig. 4f). Similarly, the computed number of dimers of the proximal four-enzyme system is only 13% higher than the distal configuration, whereas experiments indicated a 59% increase (Fig. 4f, right graph). In addition to statistical effects related to an increased number of dimerization possibilities, we speculate that the discrepancy between theoretical and experimental results points to an allosteric

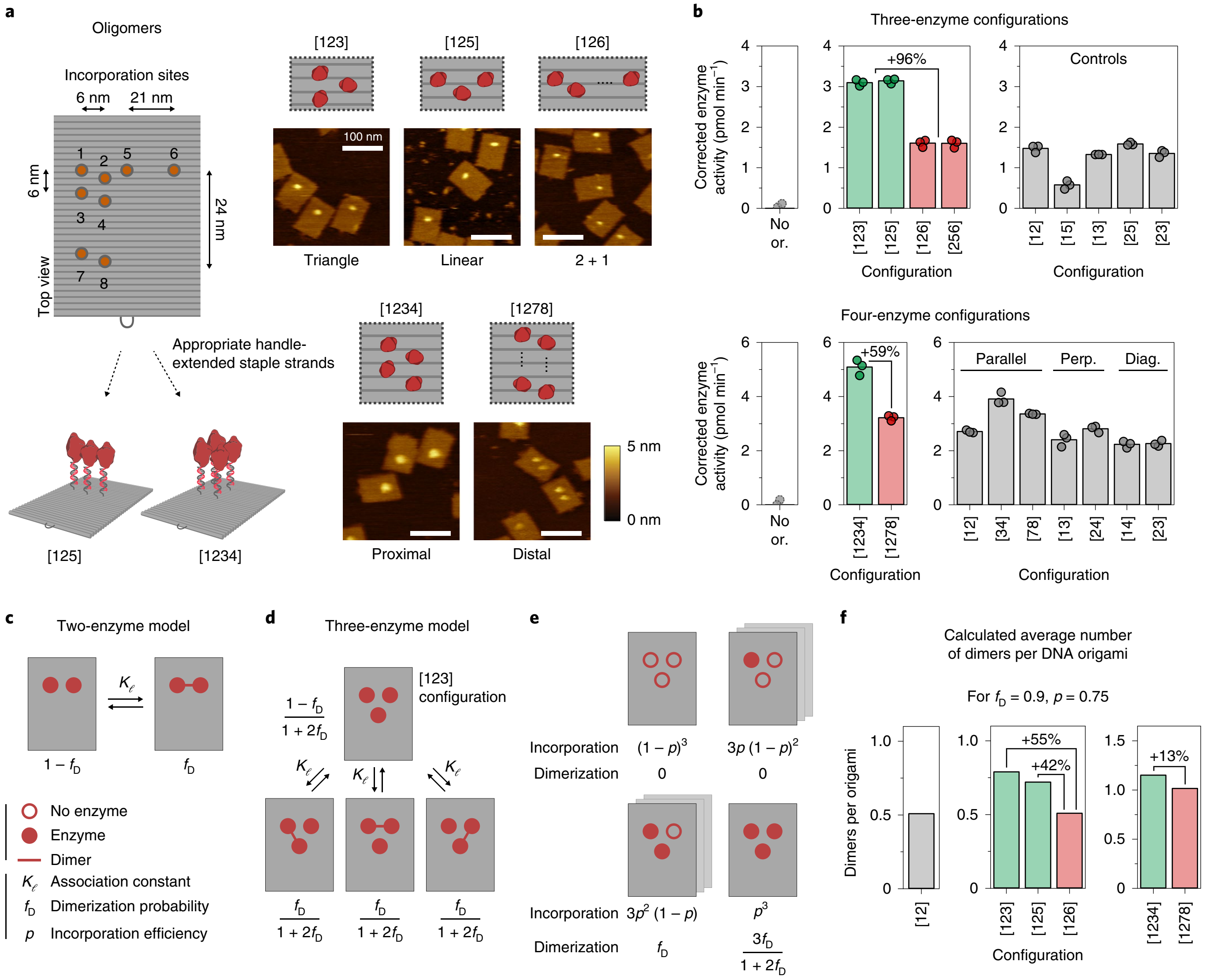

**Fig. 4 | Colocalization of more than two caspase-9 monomers leads to enhanced enzymatic activity. a**, A schematic overview of possible incorporation sites for handle-extended staple strands (orange circles) for constructing three- and four-enzyme DNA nanostructures. Topographic AFM images show successful incorporation of caspase-9 according to the pre-programmed positions. The values in parentheses indicate the enzyme configuration as determined by the number and location of the indicated incorporation sites. Colour bars indicate the height scale. Scale bars, 100 nm. **b**, Enzymatic activity measurements for three-enzyme (top) and four-enzyme (bottom) DNA nanostructures (multivalent configurations in green and reference configurations in red) and two-enzyme controls (grey). Activity was corrected by subtracting the mean background activity (no or.) in all samples. No or., no DNA origami present; perp., perpendicular arrangement; diag., diagonal arrangement. **c**, A schematic depiction of the mass-balance model for a tethered two-enzyme system, with an equilibrium between a monomeric (left) and dimeric (right) state defined by effective association constant $K_\ell$, leading to $f_D$. **d**, A model for the tethered three-enzyme system in triangular configuration ([123]) (see Supplementary Note 1 for models of other configurations). One monomeric and three symmetric dimeric states can be defined, with corresponding state fractions expressed as a function of $f_D$. **e**, A schematic depiction of the possible configurations in the triangular three-enzyme system with incomplete enzyme incorporation. **f**, When taking into account all possible states and incomplete incorporation, the models predict the average number of enzyme dimers per DNA origami for all two-, three- and four-enzyme systems. Reactions were performed as described in Fig. 3. The DNA origami concentration was adjusted to keep the total concentration of enzyme at 24 nM (see Methods and Supplementary Table 3). All experiments were performed in triplicate. Individual data points are represented as circles, whereas bars represent mean activity.

effect in oligomers of three or more caspase-9 enzymes, leading to further enhancement in activity.

Taken together, this combined experimental and theoretical approach allowed us to determine the factors that contribute to caspase-9 activation in multienzyme assemblies, demonstrating an increase in enzyme activity in oligomers of more than two monomers. Importantly, we found that the presence of multiple colocalized binding sites leads to a statistical enhancement in activity by increasing the probability of interaction between tethered enzymes when enzyme occupancy is incomplete. We envision that this principle, facilitated by spatial organization of enzymes on SMOCs, could represent a general regulatory mechanism for inducing proximity-driven protein–protein interactions[4,5].

**Enzymatic activity originates from a single catalytic site.** Finally, we used the modularity of the DNA origami method to investigate

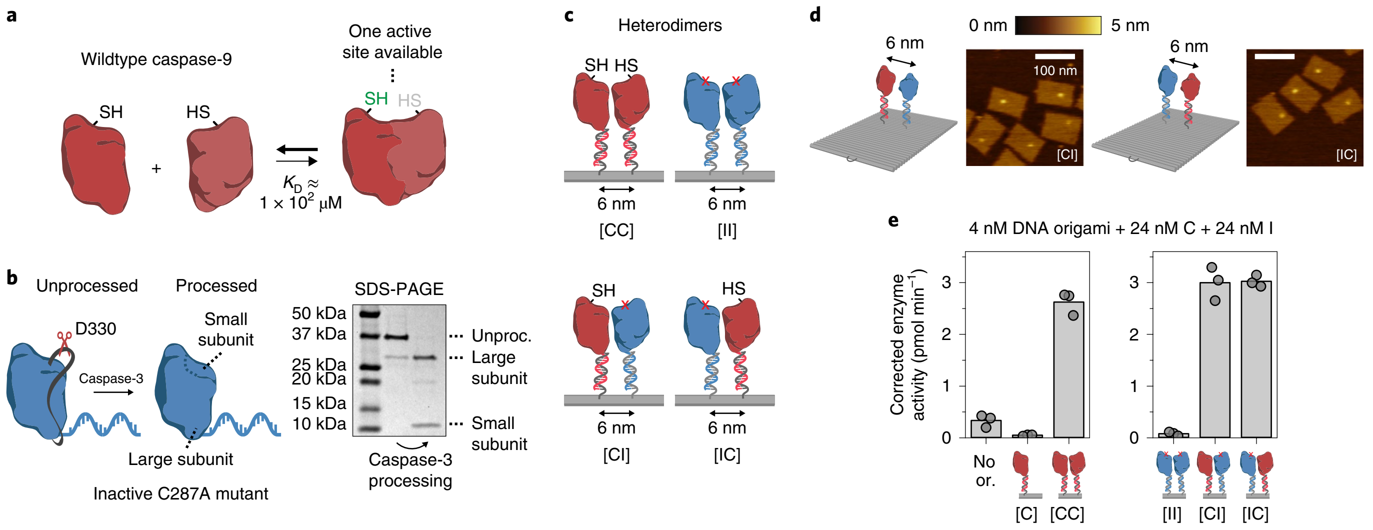

**Fig. 5 | Enzymatic activity of the caspase-9 dimer originates from a single catalytic site. a**, Schematic overview of homodimerization of C. Crystal structures of dimeric caspase-9 indicate that only one of the two active sites is in an active, accessible conformation. **b**, Wild-type caspase-9 undergoes autoproteolytic processing at three cleavage sites in the intersubunit linker region (black ribbon), but mutant I is inactive and therefore does not undergo autoprocessing. To mimic processing, enzyme–DNA conjugates were incubated with caspase-3, a constitutively active protease that also cleaves caspase-9 in the linker region. Purification was performed as described in Fig. 1, and confirmed by SDS-PAGE under reducing conditions. Label: unproc., unprocessed enzyme–DNA conjugate. **c**, The modularity of DNA origami was exploited to construct both homo- and heterodimeric 6-nm two-enzyme DNA nanostructures that consist of combinations of wild-type and inactive monomers. The specific configuration of the C and I mutants is denoted using bracket notation. **d**, Topographic AFM images of [CI] and [IC] heterodimers are shown. The colour bar indicates the height scale. Scale bars, 100 nm. **e**, Enzymatic activity measurements were performed as described in Fig. 3. In all samples, both 24 nM C and 24 nM processed I were added (for data with unprocessed I, see Supplementary Fig. 26). Activity was corrected by subtracting the mean background activity in all samples. All experiments were performed in triplicate. Individual data points are represented as circles, whereas bars represent mean activity. No or., no DNA origami present.

assembly and activity of caspase-9 heterodimers. As the crystal structure of the caspase-9 homodimer reveals that only one of the two active sites is in an accessible, open conformation[38], we hypothesized that a heterodimer that consists of a wild-type monomer and a mutant with a disabled active site would still display enzymatic activity (Fig. 5a). Recent work suggests that autoproteolytic processing of the intersubunit linker in wild-type caspase-9 is essential for the correct formation of an active dimeric state[51]. Catalytically inactive point-mutant C287A does not undergo autoproteolytic processing, and therefore we induced processing using caspase-3, which is able to cleave caspase-9 in the intersubunit linker to generate the large and small enzyme subunit (Fig. 5b and Supplementary Fig. 5)[54]. We then used wild-type caspase-9 monomer, C, and inactive monomer, I, to assemble homo- and heterodimeric two-enzyme DNA nanostructures, and confirmed that the heterodimeric variants assembled correctly using agarose gel electrophoresis (Supplementary Fig. 24) and AFM imaging (Fig. 5c,d and Supplementary Fig. 25). Remarkably, the level of protease activity of both heterodimeric systems [CI] and [IC] is equivalent to the activity of the homodimeric wild-type system [CC] (Fig. 5e). Control experiments, in which similar heterodimeric configurations were tested with unprocessed I and non-dimerizing point-mutant F404D, exhibited background activity levels (Supplementary Fig. 26). These results suggest that (1) the formation of an active caspase-9 dimer proceeds through an asymmetric mechanism in which only a single active site is brought into an active conformation and (2) that cleavage of the intersubunit linker of both monomers is strictly necessary for enzymatic activity. One of the possible mechanisms behind this half-of-sites reactivity is an absolute form of negative cooperativity between the enzyme monomers, where substrate binding in one the active sites abrogates the catalytic activity of the other site through induced conformational changes[68–70]. These experiments illustrate that the modularity of DNA origami-based platforms can be harnessed to investigate relevant biological questions concerning the molecular mechanisms behind interacting signalling proteins.

## Conclusions

Many intracellular signalling proteins assemble into multimolecular complexes composed of unique combinations of pathway components. The colocalization of proteases, kinases and phosphatases through their association to dedicated scaffold proteins results in the assembly of higher-order signalling machines such as the myddosome, apoptosome and necrosome, which are able to efficiently control signal transmission through proximity-driven enzyme activation[4,5,71]. Here we show that DNA origami can be used as a unique in vitro platform for constructing synthetic higher-order signalling machines. As a proof-of-principle, we engineered synthetic DNA origami-based variants of the apoptosome and revealed how the distance and number of caspase-9 monomers influence enzymatic activity. Our results reveal a multivalent catalytic effect as evidenced by an increase in catalytic activity in three- and four-enzyme systems compared with a two-enzyme configuration. A thermodynamic model that is based on tethered dimerization revealed that the observed activity enhancement partially originates from a statistical increase in the number of active catalytic units in higher-order enzyme configurations. We envision that clustering of catalytic enzymatic subunits into higher-order complexes, either through SMOC-based assembly[4,5], functional homotypic interactions[72,73] or via liquid phase separation[74,75], could represent a general mechanism for enzymatic activity enhancement or regulation in various intracellular processes.

In contrast with other available platforms for engineering higher-order signalling machines, such as synthetic protein scaffolds[7] or leucine zipper-induced assemblies[47], DNA origami allows oligomerization of non-identical signalling proteins and user-defined control over their number, position and relative geometry. The construction of higher-order signalling complexes using DNA origami-based SMOCs allows a detailed analysis of their function and can be used to probe unresolved molecular mechanisms in intracellular signalling, such as, for example, the multivalent enhancement of catalytic activity as reported in this work. Recent work has shown the possibility of genetically encoded DNA and RNA nanostructures and revealed successful intracellular assembly of a simple DNA cross-over nanostructure on which proteins could be organized using orthogonal zinc fingers[76–78]. As such, in vivo production and assembly of DNA-based SMOCs, analogous to those developed by us, is a realistic possibility and could find application as modular synthetic control elements for diversifying signalling dynamics of existing pathways. We anticipate that DNA origami platforms will find broad use to inform the function of many other important SMOCs for which oligomerization-driven allosteric regulation of non-identical enzymes, such as for example kinases, is a common regulatory principle.

## Methods

**Expression and purification of caspase-9.** The catalytic domain of human caspase-9 (140–416) with an N-terminal amber stop codon was encoded on a pET28a plasmid and synthesized by GenScript. The construct contains an N-terminal His-SUMO tag (the small ubiquitin-like modifier (SUMO) tag was included to improve stability and solubility during expression) and a C-terminal Strep-tag (see Supplementary Methods, DNA and protein sequence caspase-9). The C287A and F404D mutants were generated using the QuikChange Lightning Multi Site-Directed Mutagenesis kit (Agilent), according to the manufacturer's instructions and using the primers in Supplementary Table 1. The pEVOL-pAzF vector, encoding for the orthogonal aminoacyl tRNA synthetase/tRNA pair, was a kind gift from Peter Schultz (Addgene plasmid no. 31186). Both plasmids were transformed into *E. coli* BL21(DE3) competent bacteria (Novagen) and cultured at 37 °C in 500 ml 1× TB (terrific broth, VWR) supplemented with 0.4% (v/v) glycerol, 25 μg ml$^{-1}$ kanamycin and 25 μg ml$^{-1}$ chloramphenicol. Protein expression was induced at $OD_{600} = 0.6$ by addition of 1 mM β-D-1-thiogalactopyranoside and 0.02% (w/v) arabinose. Simultaneously, the non-canonical amino acid *p*-azidophenylalanine was added directly to the culture medium at a final concentration of 1 mM. Expression was carried out for ~16 h at 18 °C. Cells were harvested by centrifugation at 10,000 g for 10 min at 4 °C, the pellet resuspended in lysis buffer (10 ml per gram pellet, 1× PBS, 370 mM NaCl, 10% (v/v) glycerol, 20 mM imidazole, Benzonase nuclease (25 U per 10 ml buffer, Novagen), pH 7.4) and the cells were lysed using an EmulsiFlexC3 High Pressure homogenizer (Avestin) at 15,000 psi for two rounds. The soluble fraction (cleared lysate) that contained caspase-9 was collected by centrifugation at 40,000 g for 30 min at 4 °C.

Typically, non-canonical amino acids are not fully incorporated, which leads to the presence of truncated protein fragments. Therefore, purification was performed by both $Ni^{2+}$-affinity chromatography and *Strep*-tactin affinity chromatography, using the N- and C-terminal affinity tags on caspase-9, respectively. The cleared lysate was loaded on a nickel-charged column (His•Bind Resin, Novagen), washed with wash buffer (1x PBS, 370 mM NaCl, 10% (v/v) glycerol, 20 mM imidazole, pH 7.4), and eluted with elution buffer (1x PBS, 370 mM NaCl, 10% (v/v) glycerol, 250 mM imidazole, pH 7.4). Cleavage of the N-terminal His-SUMO tag was performed by adding SUMO protease dtUD1 (1:500, purified according to standard procedure[79]) and 2 mM EDTA to the elution fractions, while dialysing (molecular weight cut-off (MWCO) 3.5 kDa, Thermo Fisher) against 4 l of dialysis buffer (50 mM Tris, 150 mM NaCl, pH 8.0) for ~16 h at 4 °C. Finally, the concentrate was applied to a *Strep*-tactin column (Superflow resin, IBA Life Sciences). The column was washed with wash buffer (100 mM Tris-HCl, 150 mM NaCl, 1 mM EDTA, pH 8.0) and the protein eluted with wash buffer supplemented with 2.5 mM desthiobiotin. Elution fractions were combined and concentrated using Amicon 10 kDa MWCO centrifugal filters (Merck Millipore) to a final concentration of ~1.5 mg ml$^{-1}$ (~47 μM) and then snap frozen in liquid nitrogen and stored in 100 μl aliquots at −80 °C. The concentration of caspase-9 was determined by measuring the absorption at 280 nm (NanoDrop 1000, Thermo Scientific) assuming an extinction coefficient of $3.1 \times 10^4$ M$^{-1}$ cm$^{-1}$ (ref. [80]). The total yield after purification typically was ~4 mg l$^{-1}$ culture medium. Purity of caspase-9 was assessed using SDS-PAGE under reducing conditions (Supplementary Fig. 1). The molecular weight was confirmed using liquid chromatography quadrupole time-of-flight mass spectrometry (Waters ACQUITY UPLC I-Class System coupled to a Xevo G2 Q-ToF) by injecting a 0.1 μl sample into an Agilent Polaris C18A reversed-phase column with a flow of 0.3 ml min$^{-1}$ and a 15–60% acetonitrile gradient containing 0.1% formic acid (Supplementary Fig. 2).

**Enzyme–DNA conjugation.** The functionalization of amino-modified oligonucleotides with BCN is described in the Supplementary Methods 'Functionalization of oligonucleotides' section. Before conjugation, 100 μl caspase-9 aliquots were buffer exchanged to wash buffer (100 mM Tris-HCl, 150 mM NaCl, 1 mM EDTA, pH 8.0) using Zeba desalting columns (7 kDa MWCO, 0.5 ml, Thermo Scientific) according to the manufacturer's instructions to remove all of the remaining desthiobiotin. Typically, conjugation reactions were carried out on a 500 μl scale using 10 μM protein and 30 μM BCN–DNA in reaction buffer (100 mM Tris-HCl, 150 mM NaCl, 1 mM EDTA, 0.1% CHAPS (w/v), pH 8.0) for ~16 h at 4 °C. Thiol–yne reactions of BCN–DNA that competed with the 11 cysteines in caspase-9 were suppressed by preincubating the protein with 1 mM β-mercaptoethanol for 30 min at 4 °C (ref. [81]). For the proteolytic processing of C287A and F404D mutants, 0.5 μM active caspase-3 (expressed and purified as described[82]) was added directly after the conjugation reaction and incubated for 2 h at 18 °C.

To remove excess BCN–DNA, *Strep*-tactin affinity chromatography was performed as described above. Then, ion-exchange chromatography was performed to remove unreacted protein. After equilibration of the ion-exchange column (0.5 ml strong anion-exchange spin columns, Thermo Scientific) with purification buffer (100 mM Tris-HCl, 150 mM NaCl, 1 mM EDTA, 1 mM DTT, 0.1% CHAPS (w/v), pH 8.0), the protein mixture was directly loaded onto the column in 400 μl fractions, according to the manufacturer's instructions. Elution was performed by stepwise increase of the NaCl concentration in the buffer (at 200, 300, 400, 500, 600 mM, in turn). Typically, the protein eluted at < 300 mM NaCl, whereas enzyme–DNA conjugates eluted at 500–600 mM NaCl (Supplementary Figs. 4 and 5). Elution fractions containing pure enzyme–DNA conjugates were pooled, supplemented with glycerol (5% (v/v) final concentration), snap frozen in liquid nitrogen and stored at −80 °C in 5 μl aliquots. The concentration of purified enzyme–DNA conjugates was determined with gel densitometry on SDS-PAGE. To this end, conjugate gel band intensity was determined using the ImageJ (v.1.52n) gel analysis plugin and then compared to a calibration curve of known concentrations of protein (Supplementary Fig. 7).

**Assembly of caspase-9 on template T.** The linear 30-nt single-stranded template T was designed to act as a bivalent scaffold for caspase-9 (5' to 3': TCATACGACTCACTCCTGACTGACTGACTG), simultaneously hybridizing to enzyme–DNA conjugates with anti-handle sequences a1 and a2 (Supplementary Table 2), similar to designs used in the literature[46,83]. Activation of caspase-9 with template T was performed by adding the two caspase-9 enzyme–DNA conjugates and template T in equimolar amounts (4 nM) for 2 h at 4 °C in activity buffer (10 mM Tris, 1 mM EDTA, 10 mM $MgCl_2$, 100 mM NaCl, 1 mM DTT, 0.1% (w/v) CHAPS, pH 7.5). Enzyme activity was measured as described below.

**Assembly of caspase-9 on DNA origami.** The DNA origami rectangle used in this study was based on the tall rectangle design by Rothemund[18]. Staple strands and handle-extended staple strands were obtained in desalted form from Integrated DNA Technologies and dissolved at a stock concentration of 500 μM in DNase/RNase-free water. The M13mp18 scaffold was purchased from Eurofins. Folding was performed on a 25-nM scaffold scale and purification was performed according to standard procedure using 100 kDa MWCO 0.5 ml Amicon centrifugal filters (Merck Millipore). See Supplementary Methods for detailed notes on design and assembly of DNA origami nanostructures, and characterization with gel electrophoresis and AFM imaging

Incorporation of enzyme–DNA conjugates onto purified DNA origami nanostructures was performed by incubating DNA origami with 3 molar equivalents of caspase-9 DNA conjugate per handle for 2 h at 4 °C in activity buffer (10 mM Tris, 1 mM EDTA, 10 mM $MgCl_2$, 100 mM NaCl, 1 mM DTT, 0.1% (w/v) CHAPS, pH 7.6). The total concentration of caspase-9 DNA conjugate was kept constant at 24 nM for all experiments, reflecting typical concentrations in the cytosol[34]. As a result, 4 nM, 2.67 nM, and 2 nM DNA origami was used for two-, three- and four-enzyme DNA nanostructures, respectively. All experiments in the top row of Fig. 4b including the two-enzyme configurations, were performed with 2.67 nM DNA origami (for an overview of component concentrations, see Supplementary Table 3) to allow comparison of the activity of three-enzyme DNA nanostructures with two-enzyme controls. For heterodimer experiments, the concentration of each enzyme–DNA conjugate was kept at 24 nM, which results in the same background activity originating from wild-type caspase-9. For inhibition experiments, varying concentrations of XIAP (human recombinant BIR3-XIAP, R&D Systems) were added after caspase-9 incorporation and the reaction was further incubated for 1 h at 4 °C before measuring enzyme activity at 18 °C, as described below.

**Activity assays.** Enzyme activity was measured using the synthetic tetrapeptide caspase-9 substrate LEHD (dissolved in dry DMSO at 10 mM)[47], which is cleaved by caspase-9 after the aspartic acid residue releasing and unquenching the fluorescent dye AFC. After assembly of caspase-9 on DNA origami, substrate was added to a final concentration of 167 μM and proteolytic cleavage was monitored over time in 384-well plates (60 μl reaction volume) at 18 °C by measuring fluorescence (excitation: 400 nm, emmission: 505 nm) in a Tecan Spark 10 M platereader. Fluorescence units were converted to concentration using a calibration curve (Supplementary Fig. 8). To this end, varying concentrations of free AFC (dissolved in dry DMSO at 10 mM) were added to activity buffer, and fluorescence was measured as described. Raw data of all activity assays were extracted, converted and formatted using in-house MATLAB scripts (R2015a). Enzyme activity (in pmol min$^{-1}$) was determined by fitting the initial slope (20–60 min) of the kinetic trace to a linear curve. Kinetic parameters were determined by measuring enzyme activity as a function of varying LEHD concentration between 0–1.5 mM, and fitting the results with the standard Michaelis–Menten equation:

$$\text{Activity} = \frac{V_{\max}[\text{LEHD}]}{K_{\text{M}} + [\text{LEHD}]} \tag{1}$$

with $V_{\max}$ the maximum rate (in pmol min$^{-1}$) and $K_{\text{M}}$ the Michaelis constant (in mM). Because high concentrations of the substrate (>0.5 mM) strongly influence the pH, kinetic analyses were performed at a higher buffer concentration (50 mM HEPES, 5 mM Tris, 1 mM EDTA, 10 mM $MgCl_2$, 100 mM NaCl, 1 mM DTT, 0.1% (w/v) CHAPS, pH 7.6).

**Data processing and correction.** Typically, an excess of caspase-9 enzyme–DNA conjugate was used to incorporate caspase-9 onto DNA nanostructures, leading to background activity that originates from untethered enzymes remaining in solution. In some cases background correction was performed by measuring the activity of untethered caspase-9 without DNA origami, at the same concentration as in measurements with DNA origami, in triplicate and in parallel for each experiment (indicated by no origami). The mean activity was subsequently subtracted from the enzyme activity of other samples, leading to the corrected enzyme activity, as reported in Figs. 3b, 4b and 5e. The corrected enzyme activity for one-enzyme (see Fig. 5e) and two-enzyme DNA nanostructures at large monomer separation (>20 nm, see Fig. 3b) is similar to the negative controls (no origami and no handles; see Fig. 3b), suggesting that untethered caspase-9 in solution does not interact with or influence the behaviour of caspase-9 on DNA nanostructures.

To compare activation of caspase-9 on DNA nanostructures with bivalent template T as reported in Fig. 3c, activity normalization was performed. Due to incomplete enzyme incorporation (75% per handle, as determined in Fig. 2), only ~56% (or ~2.3 nM) of the two-enzyme DNA nanostructures contain two enzymes and are therefore in an active state. Because the enzyme activity of caspase-9 on DNA nanostructures is concentration independent, the corrected enzyme activity was normalized to 100% enzyme incorporation (or 4 nM DNA origami), leading to the normalized enzyme activity as reported in Fig. 3c. Assuming quantitative assembly of caspase-9 on template T (melting temperature >40 °C for 15-nt handle–anti-handle duplexes at 4 nM, ref. [84]), this allows comparison of the activity of caspase-9 assembled on either DNA origami or 4 nM template T. The fold change in Fig. 3c was calculated based on the untethered enzyme activity of 4 nM caspase-9 in solution (indicated by non-tet.).

**Geometric model.** Molecular dynamics simulations were performed to determine tethered handle–anti-handle movement on the DNA origami surface using oxDNA (v.2.2.2), a robust coarse-grained molecular dynamics model that is specifically optimized for the accurate modelling of DNA nanostructures (see the molecular dynamics simulations section of the Supplementary Methods)[58]. A three-dimensional geometric model based on the results of these simulations was constructed using Mathematica (v.10, Wolfram). The model includes two tethered particles that are separated by a distance $s$, reflecting the experimental set-up detailed in Figs. 2 and 3a,b. The diameter of a caspase-9 monomer was estimated to be 4.5 nm based on the crystal structure (PDB: 1JXQ). The tether that connects the enzyme to the DNA origami scaffold consists of the 15-bp handle–anti-handle DNA duplex, the BCN–azide moiety, single-stranded DNA linkers and a short peptide linker, and was estimated to have a total length of approximately 8 nm (Supplementary Fig. 21). By following the approach of Van Valen et al.[64], the model allows us to calculate the probability that the tethered particles form a dimer (expressed as $f_{\text{D}}$) as a function of monomer separation ($s$) and the $K_{\text{D}}$ of dimerization in solution. The approach relies on treating the particles as point objects and assuming that the particles are free to dimerize when they are within each other's vicinity. The probability that the particles are close depends on the exact conformational movement of both particles. A particle's conformational space with volume $v_{\text{s}}$ is defined based on a hemi shell that is bounded by an angle of 35° with the scaffold, as determined by the overall movement of the handle–anti-handle duplex in the coarse-grained simulations (Supplementary Fig. 21). The intersection with volume $v_{\text{i}}(s)$ between two conformational spaces can then be calculated as a function of the separation between the two particles. Assuming the particles can move freely and homogeneously in their conformational spaces and independently of each other, we can calculate the probability $p_1(s)$ that one particle is at the intersection as

$$p_1 = \frac{v_{\text{i}}}{v_{\text{s}}} \tag{2}$$

and probability $p_2 = p_1^2$ that two particles are at the intersection. This allows us to define a probability density function

$$J(s) = \frac{p_2}{v_{\text{s}}} \tag{3}$$

as the concentration of tethered particles in each other's vicinity. Note that $J$ is expressed in units of concentration, and can therefore be viewed as an effective concentration. With this, we can write an expression for $f_{\text{D}}$ based on statistical mechanical treatment of the system[64], as

$$f_{\text{D}}(s, K_{\text{D}}) = \frac{J}{J + K_{\text{D}}} \tag{4}$$

This expression was used for the graph shown in Fig. 3d. The $K_{\text{D}}$ of non-tethered caspase-9 dimerization in solution is not known precisely but reported in the high micromolar range (>50 μM)[34], and therefore results are shown for several values of $K_{\text{D}}$ in this range.

**Reporting summary.** Further information on research design is available in the Nature Research Reporting Summary linked to this article.

## Data availability

The data that support the plots within this paper and other findings of this study are available from the corresponding author on reasonable request.

## Code availability

Custom-written code for the computer models and simulations that support the experimental findings in this study is available from the corresponding author on reasonable request.

Received: 5 June 2019; Accepted: 14 November 2019;

## References

1. Bhattacharyya, R. P., Reményi, A., Yeh, B. J. & Lim, W. A. Domains, motifs, and scaffolds: the role of modular interactions in the evolution and wiring of cell signaling circuits. *Annu. Rev. Biochem.* **75**, 655–680 (2006).
2. Park, H. H. et al. The death domain superfamily in intracellular signaling of apoptosis and inflammation. *Annu. Rev. Immunol.* **25**, 561–586 (2007).
3. Good, M. C., Zalatan, J. G. & Lim, W. A. Scaffold proteins: hubs for controlling the flow of cellular information. *Science* **332**, 680–686 (2011).
4. Wu, H. Higher-order assemblies in a new paradigm of signal transduction. *Cell* **153**, 287–292 (2013).
5. Kagan, J. C., Magupalli, V. G. & Wu, H. SMOCs: supramolecular organizing centres that control innate immunity. *Nat. Rev. Immunol.* **14**, 821–826 (2014).
6. Lin, S.-C., Lo, Y.-C. & Wu, H. Helical assembly in the MyD88–IRAK4–IRAK2 complex in TLR/IL-1R signalling. *Nature* **465**, 885–890 (2010).
7. Park, S.-H., Zarrinpar, A. & Lim, W. A. Rewiring MAP kinase pathways using alternative scaffold assembly mechanisms. *Science* **299**, 1061–1064 (2003).
8. Tan, Y. & Kagan, J. C. Innate immune signaling organelles display natural and programmable signaling flexibility. *Cell* **177**, 384–398.e11 (2019).
9. Kholodenko, B. N., Hancock, J. F. & Kolch, W. Signalling ballet in space and time. *Nat. Rev. Mol. Cell Biol.* **11**, 414–426 (2010).
10. Castellana, M. et al. Enzyme clustering accelerates processing of intermediates through metabolic channeling. *Nat. Biotechnol.* **32**, 1011–1018 (2014).
11. Lim, W. A. Designing customized cell signalling circuits. *Nat. Rev. Mol. Cell Biol.* **11**, 393–403 (2010).
12. Conrado, R. J., Varner, J. D. & DeLisa, M. P. Engineering the spatial organization of metabolic enzymes: mimicking nature's synergy. *Curr. Opin. Biotechnol.* **19**, 492–499 (2008).
13. Idan, O. & Hess, H. Engineering enzymatic cascades on nanoscale scaffolds. *Curr. Opin. Biotechnol.* **24**, 606–611 (2013).
14. Chen, Y.-J., Groves, B., Muscat, R. A. & Seelig, G. DNA nanotechnology from the test tube to the cell. *Nat. Nanotechnol.* **10**, 748–760 (2015).
15. Seeman, N. C. & Sleiman, H. F. DNA nanotechnology. *Nat. Rev. Mater.* **3**, 17068 (2017).
16. Engelen, W., Janssen, B. M. G. & Merkx, M. DNA-based control of protein activity. *Chem. Commun.* **52**, 3598–3610 (2016).
17. Fu, J., Liu, M., Liu, Y. & Yan, H. Spatially-interactive biomolecular networks organized by nucleic acid nanostructures. *Acc. Chem. Res.* **45**, 1215–1226 (2012).
18. Rothemund, P. W. K. Folding DNA to create nanoscale shapes and patterns. *Nature* **440**, 297–302 (2006).
19. Voigt, N. V. et al. Single-molecule chemical reactions on DNA origami. *Nat. Nanotechnol.* **5**, 200–203 (2010).
20. Saccà, B. & Niemeyer, C. M. Functionalization of DNA nanostructures with proteins. *Chem. Soc. Rev.* **40**, 5910–5921 (2011).
21. Udomprasert, A. et al. Amyloid fibrils nucleated and organized by DNA origami constructions. *Nat. Nanotechnol.* **9**, 537–541 (2014).
22. Xu, W. et al. A programmable DNA origami platform to organize SNAREs for membrane fusion. *J. Am. Chem. Soc.* **138**, 4439–4447 (2016).
23. Funke, J. J. et al. Uncovering the forces between nucleosomes using DNA origami. *Sci. Adv.* **2**, e1600974 (2016).

24. Le, J. V. et al. Probing nucleosome stability with a DNA origami nanocaliper. *ACS Nano* **10**, 7073–7084 (2016).
25. Ketterer, P. et al. DNA origami scaffold for studying intrinsically disordered proteins of the nuclear pore complex. *Nat. Commun.* **9**, 902 (2018).
26. Masubuchi, T. et al. Construction of integrated gene logic-chip. *Nat. Nanotechnol.* **13**, 933–940 (2018).
27. Zhao, Z. et al. Nanocaged enzymes with enhanced catalytic activity and increased stability against protease digestion. *Nat. Commun.* **7**, 10619 (2016).
28. Linko, V., Eerikäinen, M. & Kostiainen, M. A. A modular DNA origami-based enzyme cascade nanoreactor. *Chem. Commun.* **51**, 5351–5354 (2015).
29. Wilner, O. I. et al. Enzyme cascades activated on topologically programmed DNA scaffolds. *Nat. Nanotechnol.* **4**, 249–254 (2009).
30. Fu, J., Liu, M., Liu, Y., Woodbury, N. W. & Yan, H. Interenzyme substrate diffusion for an enzyme cascade organized on spatially addressable DNA nanostructures. *J. Am. Chem. Soc.* **134**, 5516–5519 (2012).
31. Timm, C. & Niemeyer, C. M. Assembly and purification of enzyme-functionalized DNA origami structures. *Angew. Chem. Int Ed.* **54**, 6745–6750 (2015).
32. Ngo, T. A., Nakata, E., Saimura, M. & Morii, T. Spatially organized enzymes drive cofactor-coupled cascade reactions. *J. Am. Chem. Soc.* **138**, 3012–3021 (2016).
33. Fu, J. et al. Multi-enzyme complexes on DNA scaffolds capable of substrate channelling with an artificial swinging arm. *Nat. Nanotechnol.* **9**, 531–536 (2014).
34. Riedl, S. J. & Salvesen, G. S. The apoptosome: signalling platform of cell death. *Nat. Rev. Mol. Cell Biol.* **8**, 405–413 (2007).
35. Hu, Q. et al. Molecular determinants of caspase-9 activation by the Apaf-1 apoptosome. *Proc. Natl Acad. Sci. USA* **111**, 16254–16261 (2014).
36. Li, Y. et al. Mechanistic insights into caspase-9 activation by the structure of the apoptosome holoenzyme. *Proc. Natl Acad. Sci. USA* **114**, 1542–1547 (2017).
37. Cheng, T. C., Hong, C., Akey, I. V., Yuan, S. & Akey, C. W. A near atomic structure of the active human apoptosome. *eLife* **5**, e17755 (2016).
38. Renatus, M., Stennicke, H. R., Scott, F. L., Liddington, R. C. & Salvesen, G. S. Dimer formation drives the activation of the cell death protease caspase 9. *Proc. Natl Acad. Sci. USA* **98**, 14250–14255 (2001).
39. Niemeyer, C. M. Semisynthetic DNA–protein conjugates for biosensing and nanofabrication. *Angew. Chem. Int. Ed.* **49**, 1200–1216 (2010).
40. Chin, J. W. et al. Addition of *p*-azido-L-phenylalanine to the genetic code of *Escherichia coli*. *J. Am. Chem. Soc.* **124**, 9026–9027 (2002).
41. Chin, J. W. Expanding and reprogramming the genetic code of cells and animals. *Annu. Rev. Biochem.* **83**, 379–408 (2014).
42. Liu, C. C. & Schultz, P. G. Adding new chemistries to the genetic code. *Annu. Rev. Biochem.* **79**, 413–444 (2010).
43. Marth, G. et al. Precision templated bottom-up multiprotein nanoassembly through defined click chemistry linkage to DNA. *ACS Nano* **11**, 5003–5010 (2017).
44. Glettenberg, M. & Niemeyer, C. M. Tuning of peroxidase activity by covalently tethered DNA oligonucleotides. *Bioconjug. Chem.* **20**, 969–975 (2009).
45. Trads, J. B., Tørring, T. & Gothelf, K. V. Site-selective conjugation of native proteins with DNA. *Acc. Chem. Res.* **50**, 1367–1374 (2017).
46. Sancho Oltra, N., Bos, J. & Roelfes, G. Control over enzymatic activity by DNA-directed split enzyme reassembly. *ChemBioChem* **11**, 2255–2258 (2010).
47. Yin, Q. et al. Caspase-9 holoenzyme is a specific and optimal procaspase-3 processing machine. *Mol. Cell* **22**, 259–268 (2006).
48. Pop, C., Timmer, J., Sperandio, S. & Salvesen, G. S. The apoptosome activates caspase-9 by dimerization. *Mol. Cell* **22**, 269–275 (2006).
49. Chao, Y. et al. Engineering a dimeric caspase-9: a re-evaluation of the induced proximity model for caspase activation. *PLoS Biol.* **3**, e183 (2005).
50. Den Hamer, A. et al. Small-molecule-induced and cooperative enzyme assembly on a 14-3-3 scaffold. *ChemBioChem* **18**, 331–335 (2017).
51. Hu, Q., Wu, D., Chen, W., Yan, Z. & Shi, Y. Proteolytic processing of the caspase-9 zymogen is required for apoptosome-mediated activation of caspase-9. *J. Biol. Chem.* **288**, 15142–15147 (2013).
52. Shiozaki, E. N., Chai, J. & Shi, Y. Oligomerization and activation of caspase-9, induced by Apaf-1 CARD. *Proc. Natl Acad. Sci. USA* **99**, 4197–4202 (2002).
53. Wu, C.-C. et al. The Apaf-1 apoptosome induces formation of caspase-9 homo- and heterodimers with distinct activities. *Nat. Commun.* **7**, 13565 (2016).
54. Huber, K. L., Serrano, B. P. & Hardy, J. A. Caspase-9 CARD: core domain interactions require a properly formed active site. *Biochem. J.* **475**, 1177–1196 (2018).
55. Saccà, B. et al. Orthogonal protein decoration of DNA origami. *Angew. Chem. Int Ed.* **49**, 9378–9383 (2010).
56. Rosier, B. J. H. M. et al. Incorporation of native antibodies and Fc-fusion proteins on DNA nanostructures via a modular conjugation strategy. *Chem. Commun.* **53**, 7393–7396 (2017).
57. Baker, M. A. B. et al. Dimensions and global twist of single-layer DNA origami measured by small-angle X-ray scattering. *ACS Nano* **12**, 5791–5799 (2018).
58. Snodin, B. E. K., Schreck, J. S., Romano, F., Louis, A. A. & Doye, J. P. K. Coarse-grained modelling of the structural properties of DNA origami. *Nucleic Acids Res.* **47**, 1585–1597 (2019).
59. Sa-Ardyen, P., Vologodskii, A. V. & Seeman, N. C. The flexibility of DNA double crossover molecules. *Biophys. J.* **84**, 3829–3837 (2003).
60. Zhang, Y., Tsitkov, S. & Hess, H. Proximity does not contribute to activity enhancement in the glucose oxidase–horseradish peroxidase cascade. *Nat. Commun.* **7**, 13982 (2016).
61. Stennicke, H. R. & Salvesen, G. S. Biochemical characteristics of caspases-3, -6, -7, and -8. *J. Biol. Chem.* **272**, 25719–25723 (1997).
62. Wingard Jr., L. B., Katchalski-Katzir, E. & Goldstein, L. *Applied Biochemistry and Bioengineering. Volume 1: Immobilized Enzyme Principles* (Academic, 1976).
63. Page, M. I. & Jencks, W. P. Entropic contributions to rate accelerations in enzymic and intramolecular reactions and the chelate effect. *Proc. Natl Acad. Sci. USA* **68**, 1678–1683 (1971).
64. Van Valen, D., Haataja, M. & Phillips, R. Biochemistry on a leash: the roles of tether length and geometry in signal integration proteins. *Biophys. J.* **96**, 1275–1292 (2009).
65. Salvesen, G. S. & Duckett, C. S. IAP proteins: blocking the road to death's door. *Nat. Rev. Mol. Cell Biol.* **3**, 401–410 (2002).
66. Shiozaki, E. N. et al. Mechanism of XIAP-mediated inhibition of caspase-9. *Mol. Cell* **11**, 519–527 (2003).
67. Zaupa, G., Scrimin, P. & Prins, L. J. Origin of the dendritic effect in multivalent enzyme-like catalysts. *J. Am. Chem. Soc.* **130**, 5699–5709 (2008).
68. Hill, T. L. & Levitzki, A. Subunit neighbor interactions in enzyme kinetics: half-of-the-sites reactivity in a dimer. *Proc. Natl Acad. Sci. USA* **77**, 5741–5745 (1980).
69. Biemann, H. P. & Koshland, D. E. Aspartate receptors of *Escherichia coli* and *Salmonella typhimurium* bind ligand with negative and half-of-the-sites cooperativity. *Biochemistry* **33**, 629–634 (1994).
70. Vivoli, M., Pang, J. & Harmer, N. J. A half-site multimeric enzyme achieves its cooperativity without conformational changes. *Sci. Rep.* **7**, 16529 (2017).
71. Csizmok, V., Follis, A. V., Kriwacki, R. W. & Forman-Kay, J. D. Dynamic protein interaction networks and new structural paradigms in signaling. *Chem. Rev.* **116**, 6424–6462 (2016).
72. Levy, E. D., Erba, E. B., Robinson, C. V. & Teichmann, S. A. Assembly reflects evolution of protein complexes. *Nature* **453**, 1262–1265 (2008).
73. Bergendahl, L. T. & Marsh, J. A. Functional determinants of protein assembly into homomeric complexes. *Sci. Rep.* **7**, 4932 (2017).
74. Banani, S. F., Lee, H. O., Hyman, A. A. & Rosen, M. K. Biomolecular condensates: organizers of cellular biochemistry. *Nat. Rev. Mol. Cell Biol.* **18**, 285–298 (2017).
75. Shin, Y. & Brangwynne, C. P. Liquid phase condensation in cell physiology and disease. *Science* **357**, eaaf4382 (2017).
76. Elbaz, J., Yin, P. & Voigt, C. A. Genetic encoding of DNA nanostructures and their self-assembly in living bacteria. *Nat. Commun.* **7**, 11179 (2016).
77. Praetorius, F. & Dietz, H. Self-assembly of genetically encoded DNA-protein hybrid nanoscale shapes. *Science* **355**, eaam5488 (2017).
78. Delebecque, C. J., Lindner, A. B., Silver, P. A. & Aldaye, F. A. Organization of intracellular reactions with rationally designed RNA assemblies. *Science* **333**, 470–474 (2011).
79. Weeks, S. D., Drinker, M. & Loll, P. J. Ligation independent cloning vectors for expression of SUMO fusions. *Protein Expr. Purif.* **53**, 40–50 (2007).
80. Gasteiger, E. et al. in *The Proteomics Protocols Handbook* 571–607 (Humana Press, 2005).
81. Tian, H., Sakmar, T. P. & Huber, T. A simple method for enhancing the bioorthogonality of cyclooctyne reagent. *Chem. Commun.* **52**, 5451–5454 (2016).
82. Den Hamer, A. et al. Bright bioluminescent BRET sensor proteins for measuring intracellular caspase activity. *ACS Sens.* **2**, 729–734 (2017).
83. Janssen, B. M. G., Engelen, W. & Merkx, M. DNA-directed control of enzyme–inhibitor complex formation: a modular approach to reversibly switch enzyme activity. *ACS Synth. Biol.* **4**, 547–553 (2015).
84. Zadeh, J. N. et al. NUPACK: Analysis and design of nucleic acid systems. *J. Comput. Chem.* **32**, 170–173 (2011).

## Acknowledgements

We thank J. van Dongen for help with the mass spectrometry analyses, N. van der Zon for initial protein expression experiments and G. Cremers for helpful discussions. The ICMS Animation Studio contributed the cartoons of DNA strands and the DNA origami structure. This work was supported by the European Research Council (project no. 677313 BioCircuit), an NWO-VIDI grant from the Netherlands Organisation for Scientific Research (723.016.003) and funding from the Ministry of Education, Culture and Science (Gravity programmes 024.001.035 and 024.003.013).

## Author contributions

B.J.H.M.R. designed the study, performed experiments, developed the geometric model, analysed the data, and wrote the manuscript. A.J.M. developed and derived the

thermodynamic model and analysed the data. B.G.A. performed and analysed all AFM measurements. J.A.L.R. performed molecular dynamics simulations. A.d.H. performed initial protein expression and provided critical input for the experiments. L.B. supervised the study and provided critical feedback on the manuscript. T.F.A.d.G. conceived, designed and supervised the study, analysed the data and wrote the manuscript. All authors discussed the results and commented on the manuscript.

## Competing interests

The authors declare no competing interests.

## Additional information

**Supplementary information** is available for this paper at https://doi.org/10.1038/s41929-019-0403-7.

**Correspondence and requests for materials** should be addressed to L.B. or T.F.A.d.G.

nature research

Corresponding author(s): Tom de Greef
Luc Brunsveld

Last updated by author(s): 2019-30-10

# Reporting Summary

Nature Research wishes to improve the reproducibility of the work that we publish. This form provides structure for consistency and transparency in reporting. For further information on Nature Research policies, see Authors & Referees and the Editorial Policy Checklist.

## Statistics

For all statistical analyses, confirm that the following items are present in the figure legend, table legend, main text, or Methods section.

| n/a | Confirmed | |
|---|---|---|
| ☐ | ☒ | The exact sample size (*n*) for each experimental group/condition, given as a discrete number and unit of measurement |
| ☐ | ☒ | A statement on whether measurements were taken from distinct samples or whether the same sample was measured repeatedly |
| ☒ | ☐ | The statistical test(s) used AND whether they are one- or two-sided<br>*Only common tests should be described solely by name; describe more complex techniques in the Methods section.* |
| ☒ | ☐ | A description of all covariates tested |
| ☐ | ☒ | A description of any assumptions or corrections, such as tests of normality and adjustment for multiple comparisons |
| ☐ | ☒ | A full description of the statistical parameters including central tendency (e.g. means) or other basic estimates (e.g. regression coefficient) AND variation (e.g. standard deviation) or associated estimates of uncertainty (e.g. confidence intervals) |
| ☒ | ☐ | For null hypothesis testing, the test statistic (e.g. *F*, *t*, *r*) with confidence intervals, effect sizes, degrees of freedom and *P* value noted<br>*Give P values as exact values whenever suitable.* |
| ☒ | ☐ | For Bayesian analysis, information on the choice of priors and Markov chain Monte Carlo settings |
| ☒ | ☐ | For hierarchical and complex designs, identification of the appropriate level for tests and full reporting of outcomes |
| ☒ | ☐ | Estimates of effect sizes (e.g. Cohen's *d*, Pearson's *r*), indicating how they were calculated |

*Our web collection on statistics for biologists contains articles on many of the points above.*

## Software and code

Policy information about availability of computer code

| | |
|---|---|
| Data collection | caDNAno v0.2.4 (DNA origami design and DNA sequence generation)<br>Igor Pro v6.3.4.1 and Asylum Research v12 (AFM)<br>Tecan SparkControl v2.1 (fluorescence measurements)<br>GE Healthcare ImageQuant Capture v.1.0.2 (gel electrophoresis)<br>Thermo Xcalibur v2.2 (MS DNA)<br>Waters MassLynx v4.1 (MS proteins)<br>oxDNA v2.2.2 (MD simulations)<br>NanoDrop ND-1000 v3.5.2 (concentration determination) |
| Data analysis | Python v2.7.12 (MD analysis)<br>VMD v1.9.3 (MD visualisations)<br>MATLAB R2015a, R2016b (data extraction, AFM image processing, thermodynamic model)<br>Wolfram Mathematica v10 (geometric model)<br>ImageJ v1.52n (gel electrophoresis and AFM analysis)<br>Gwyddion v2.52 (AFM image processing)<br>Origin v2015 (plotting and data fitting)<br>MagTran v1.03 (MS deconvolution) |

For manuscripts utilizing custom algorithms or software that are central to the research but not yet described in published literature, software must be made available to editors/reviewers. We strongly encourage code deposition in a community repository (e.g. GitHub). See the Nature Research guidelines for submitting code & software for further information.

## Data

Policy information about availability of data

All manuscripts must include a data availability statement. This statement should provide the following information, where applicable:

- Accession codes, unique identifiers, or web links for publicly available datasets
- A list of figures that have associated raw data
- A description of any restrictions on data availability

All raw data are available from the corresponding authors upon request. There are no restrictions on data availability.

# Field-specific reporting

Please select the one below that is the best fit for your research. If you are not sure, read the appropriate sections before making your selection.

☒ Life sciences ☐ Behavioural & social sciences ☐ Ecological, evolutionary & environmental sciences

For a reference copy of the document with all sections, see nature.com/documents/nr-reporting-summary-flat.pdf

# Life sciences study design

All studies must disclose on these points even when the disclosure is negative.

| | |
|---|---|
| Sample size | No statistical methods were used to predetermine sample size. We performed fluorescence measurements in triplicate, and found the sample size adequate as the data was reproducible, as indicated. For determination of incorporation efficiency (Suppl. Fig. 16) at least 4 AFM images per sample were recorded in different locations on the mica substrate. In most cases, 2 separate samples were prepared and measured on separate days. At least 260 DNA origami structures were analysed per sample, which we deemed sufficient based on the small standard deviation of the incorporation efficiency between different images and typical sample sizes reported for similar analyses in literature. |
| Data exclusions | AFM images that could not be recorded with sufficient resolution (for example when the tip was not sharp enough) were excluded from analysis. DNA origami structures that were not well-formed or damaged, or structures that were only partially visible were excluded from analysis. No other data was excluded. |
| Replication | All attempts at reproducing the results in this study were successful. For fluorescence measurements in Fig. 1 and Fig. 3, independent triplicate measurements were performed on separate days, with freshly prepared DNA origami and fresh enzyme-DNA conjugate aliquots thawed immediately prior to the start of the experiment. For Fig. 4 and Fig. 5, measurements were performed in triplicate, with freshly prepared DNA origami and fresh enzyme-DNA conjugate aliquots. |
| Randomization | No randomization was done, because this study does not involve animals or human participants. |
| Blinding | No blinding was done, because this study does not involve animals or human participants. |

# Reporting for specific materials, systems and methods

We require information from authors about some types of materials, experimental systems and methods used in many studies. Here, indicate whether each material, system or method listed is relevant to your study. If you are not sure if a list item applies to your research, read the appropriate section before selecting a response.

## Materials & experimental systems

| n/a | Involved in the study |
|---|---|
| ☒ | ☐ Antibodies |
| ☒ | ☐ Eukaryotic cell lines |
| ☒ | ☐ Palaeontology |
| ☒ | ☐ Animals and other organisms |
| ☒ | ☐ Human research participants |
| ☒ | ☐ Clinical data |

## Methods

| n/a | Involved in the study |
|---|---|
| ☒ | ☐ ChIP-seq |
| ☒ | ☐ Flow cytometry |
| ☒ | ☐ MRI-based neuroimaging |